Electronic Supporting Information

Highly efficient utilization of polypyrrole enabled by dispersed buckypaper tape

for high performance flexible energy storage

Haihan Zhou*, Shaozhen Liu, Mengyao Ren, and Hua-Jin Zhai*

Key Laboratory of Materials for Energy Conversion and Storage of Shanxi Province,

Key Laboratory of Chemical Biology and Molecular Engineering of Ministry of

Education, Institute of Molecular Science, Shanxi University, Taiyuan 030006, China

*Corresponding Authors

E-mail: hhzhou@sxu.edu.cn, hj.zhai@sxu.edu.cn

Experimental section

Materials

The BP was purchased from Soochow Hengqiu Tech. Inc., whose preparation method is floating catalyst chemical vapor deposition. Both pyrrole and lithium perchlorate trihydrate were purchased from Aladdin Chemistry. All other reagents were of analytical grade and used without further purification. The deionized water with electrical resistivity of 18.25 MΩ cm at 25°C was used for all the experiments.

Preparation of DBPT

As shown schematically in Fig. 1a, 3M adhesive tape serving as support was adhered to one side of BP to obtain BPT electrodes. DBPT was prepared from BPT through anodic processes. Specifically, BPT acting as working electrode was placed in a three-electrode configuration with 0.5 M H_2SO_4 as electrolyte. The saturated calomel electrode (SCE) and Pt foil served as reference and auxiliary electrodes, respectively. An anodic process based on cyclic voltammetry (CV) was performed at a scan rate of 80 mV s^{-1} between the potentials of 1.2 and 2.0 V for 30 cycles. For comparison, BPT was also treated by a cathodic process, during which CV was implemented at 80 mV s^{-1} between the potentials of −2.0 and −1.2 V in 1 M KOH aqueous solution for 30 cycles. To remove residues, all the products were rinsed with acetone and deionized water, successively.

Electropolymerization loading of PPy

The DBPT was used as electrode substrate to load PPy by an electropolymerization route. Here a three-electrode cell equipped with a SCE reference electrode and a Pt foil counter electrode was used. The DBPT electrode substrate with a whole size of 20 mm × 10 mm served as the working electrode, and its conductive area was 10 mm × 10 mm. 2 mA cm^{-2} of current density was used for 4000 s in the aqueous solution composed of 0.2 M pyrrole and 0.1 M LiClO$_4$. For comparison, BPT/PPy electrodes were fabricated with BPT as electrode substrate through the same procedure.

Materials characterizations

Field-emission scanning electron microscopy (SEM, JSM 6701F, JEOL) and high resolution transmission electron microscopy (TEM, JEM-2100, JEOL) were applied to capture the morphologies of the samples. X-ray photoelectron spectroscopy (XPS, ESCALEAB 250Xi, ThermoFisher Scientific) tests were carried out on a XPS spectrometer with a monochromated Al Kα excitation source (λ = 8.34 Å). X-ray diffraction (XRD) patterns were obtained on an X-ray diffractometer (Ultima IV, Rigaku) with Cu Kα radiation (λ = 1.5406 Å). Raman spectra were obtained through a Raman spectrometer (DXR, ThermoFisher Scientific) with a 633 nm laser source. Surface topography was probed by an atomic force microscope (AFM, MultiMode 8, Bruker) and the NanoScope Analysis software was applied to calculate the root mean square (RMS) roughness of samples. Water contact angle was measured by a drop shape analyzer (DSA 100, Krüss). Fourier transform infrared (FTIR) spectra tests were

performed on an FTIR spectrometer (Tensor 27, Bruker). The nitrogen adsorption/ desorption isotherms were obtained by a surface area and porosity analyzer (ASAP 2460, Micromeritics) at 77 K. The specific surface area was calculated from the Brunauer-Emmett-Teller (BET) method according to N_2 adsorption data. Prior to adsorption measurements, all the samples were degassed at 393 K for 8 h. The tensile properties were measured using an electronic universal testing machine (UTM2203, SUNS) at a constant strain speed of 3 mm min^{-1}, equipped with a 2000 N load cell in elongation mode. UV-vis absorption spectra of methyl orange solutions (8 mg L^{-1}) were obtained by a UV-vis spectrometer (U4150, Hitachi) before and after the adsorption with BP and DBP for 24 h, respectively. Mass loading of PPy was measured on a MS105DU Mettler-Toledo microbalance with an accuracy of 10 μg.

Electrochemical measurements

An electrochemical workstation (CHI 660E, Chenhua) was applied to character the electrochemical performances of electrodes and SC. The electrodes were tested in a three-electrode cell, which included 1 M KCl aqueous solution, a SCE as the reference electrode, and a Pt foil as the counter electrode. The CV curves and galvanostatic charge-discharge (GCD) plots were recorded to assess the electrochemical capacitive behaviors and to calculate the specific capacitances. Electrochemical impedance spectroscopy (EIS) measurements were carried out within the frequency range from 10^5 to 10^{-2} Hz, with an AC perturbation of 5 mV versus open circuit potential.

The quasi-solid-state SC was assembled by wrapping PVA-H_2SO_4 gel electrolyte

with two symmetric electrodes. For the preparation of gel-type electrolyte, 1 g of PVA (M_w = 86,000) was added into 10 ml of 1.0 M H_2SO_4 solution, after which a vigorous stir was performed under 85°C for 1 hour until the solution became clear. Two symmetric electrodes were sandwiched together with gel electrolyte in between, until the electrolyte solidified in ambient environment. The resultant SC was tested by a two-electrode system.

The areal capacitance (C_a, mF cm^{-2}) of electrodes was calculated from the CV and GCD curves using Eqs. S1 and S2, respectively.

$$C_a = (\int idV)/(2 \times A \times v \times \Delta V) \qquad\qquad (S1)$$

$$C_a = (I \times \Delta t)/(A \times \Delta V) \qquad\qquad (S2)$$

where $\int idV$, A, v, ΔV in Eq. S1 represent the integrated area enclosed by the CV curve, electrode area in cm^{-2}, scan rate in V s^{-1}, and potential window tested in V, respectively. I and Δt in Eq. S2 represent the discharge current in mA and discharge time in s, respectively.

The areal specific energy density (E, Wh cm^{-2}) and power density (P, W cm^{-2}) of the SCs can be calculated by Eqs. S3 and S4, respectively:

$$E = (C_a \times \Delta V^2)/2 \qquad\qquad (S3)$$

$$P = E/t \qquad\qquad (S4)$$

where ΔV and t represent the potential window subtracting IR drop in V and discharge time in h, respectively.

The loading efficiency (η) of electrode substrate is calculated based on Eq. S5:

$$\eta = m_a/m_t \qquad\qquad (S5)$$

where m_a is the mass of active materials, and m_t is the total mass of active materials plus
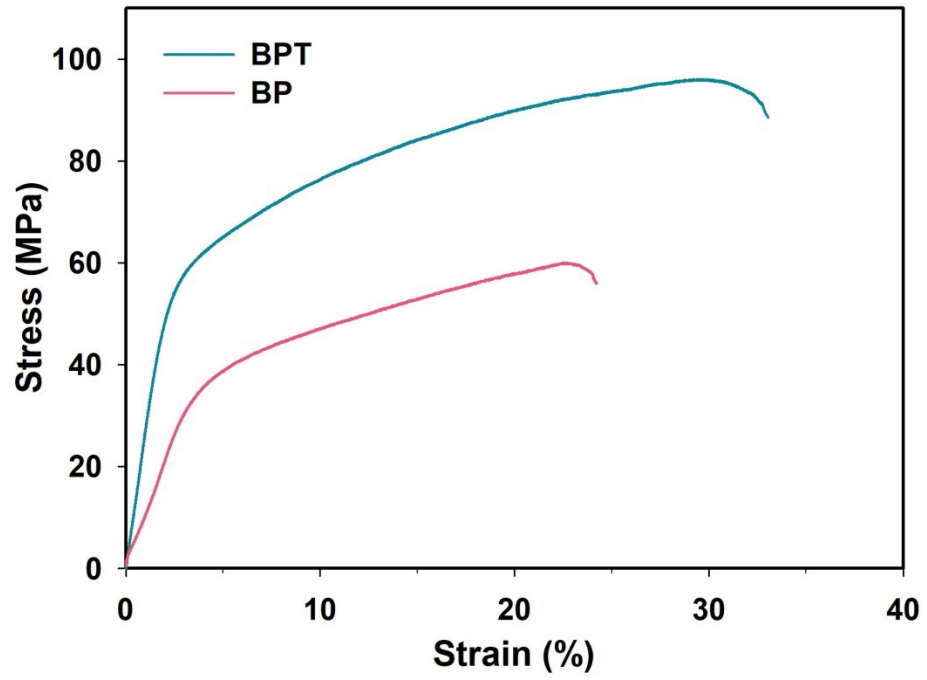
electrode substrate.
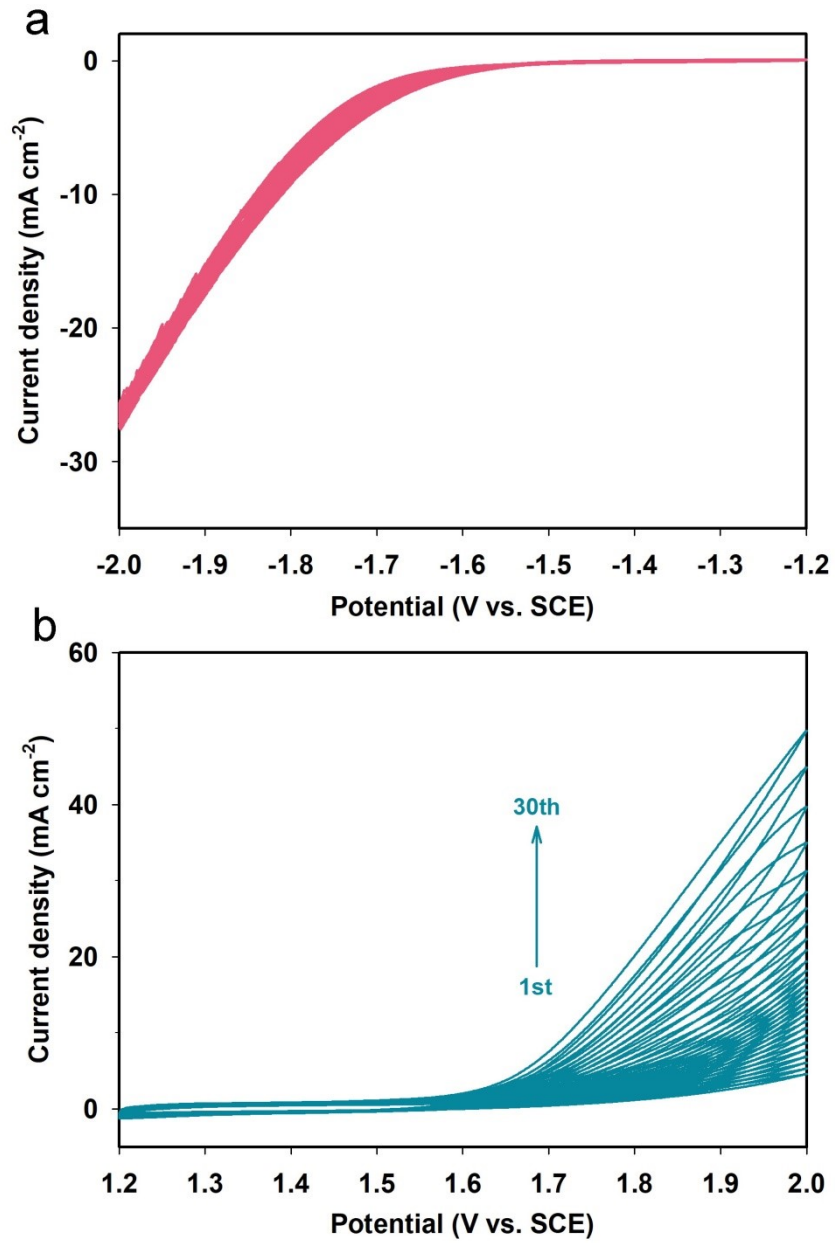
Fig. S1 Tensile stress-strain curves of BP and BPT.

Fig. S2 CV curves of BPT electrodes treated by (a) cathodic and (b) anodic processes from cycle 1 to cycle 30.
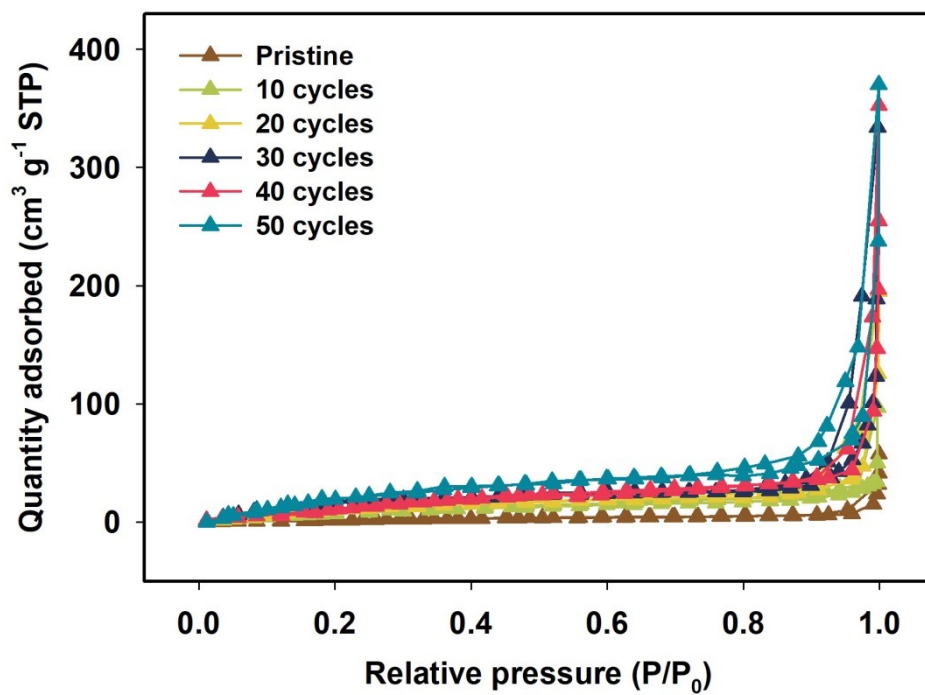
Fig. S3 N_2 adsorption/desorption isotherms of BPT (pristine) and DBPT obtained by varying CV cycles.
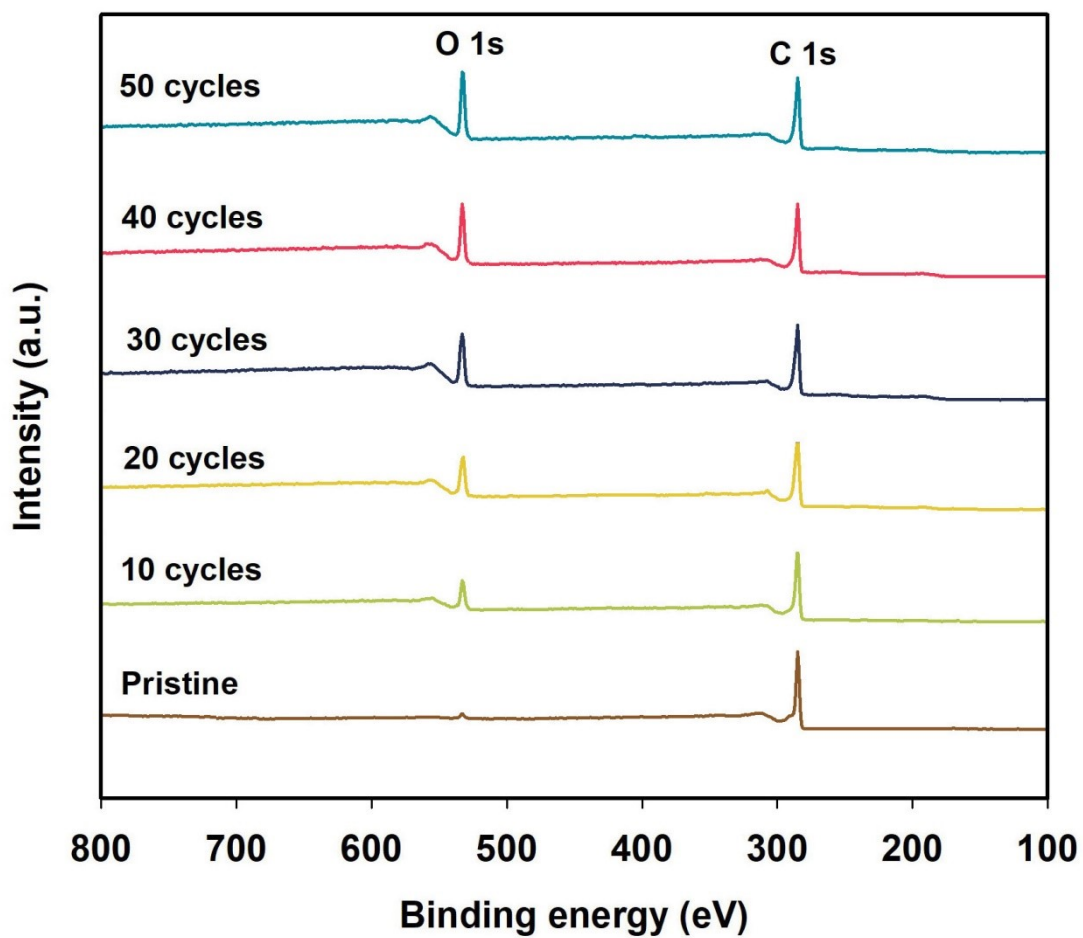
Fig. S4 XPS survey spectra of BPT (pristine) and DBPT obtained by the treatment of varying CV cycles.
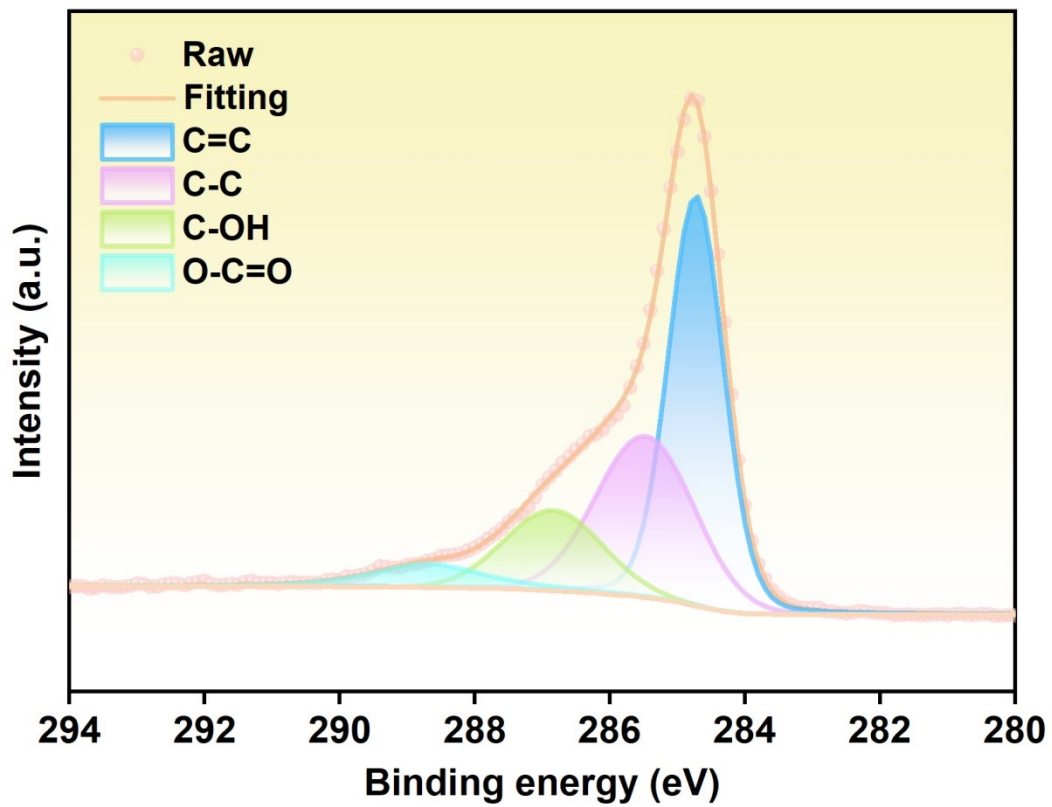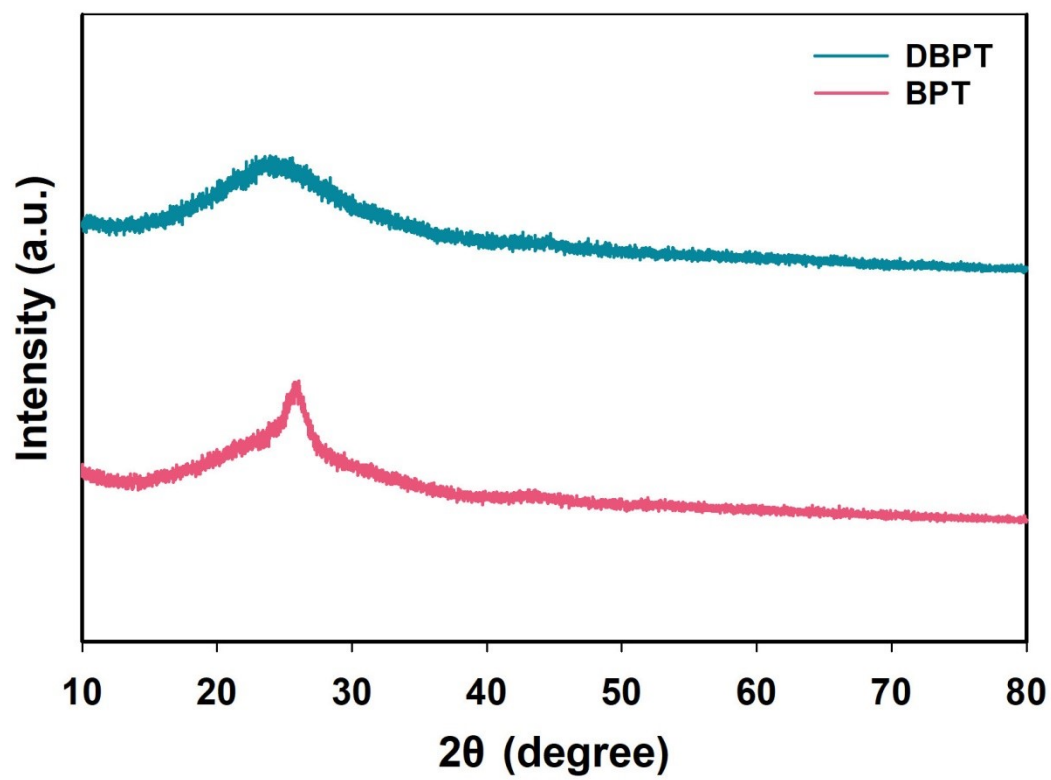
Fig. S5 The C 1s XPS spectrum of DBPT.
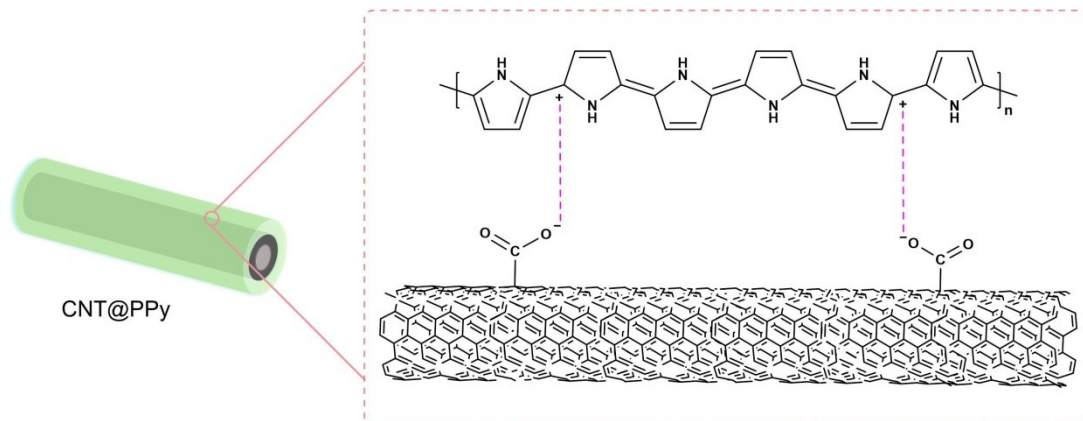
Fig. S6 XRD patterns of DBPT and BPT.

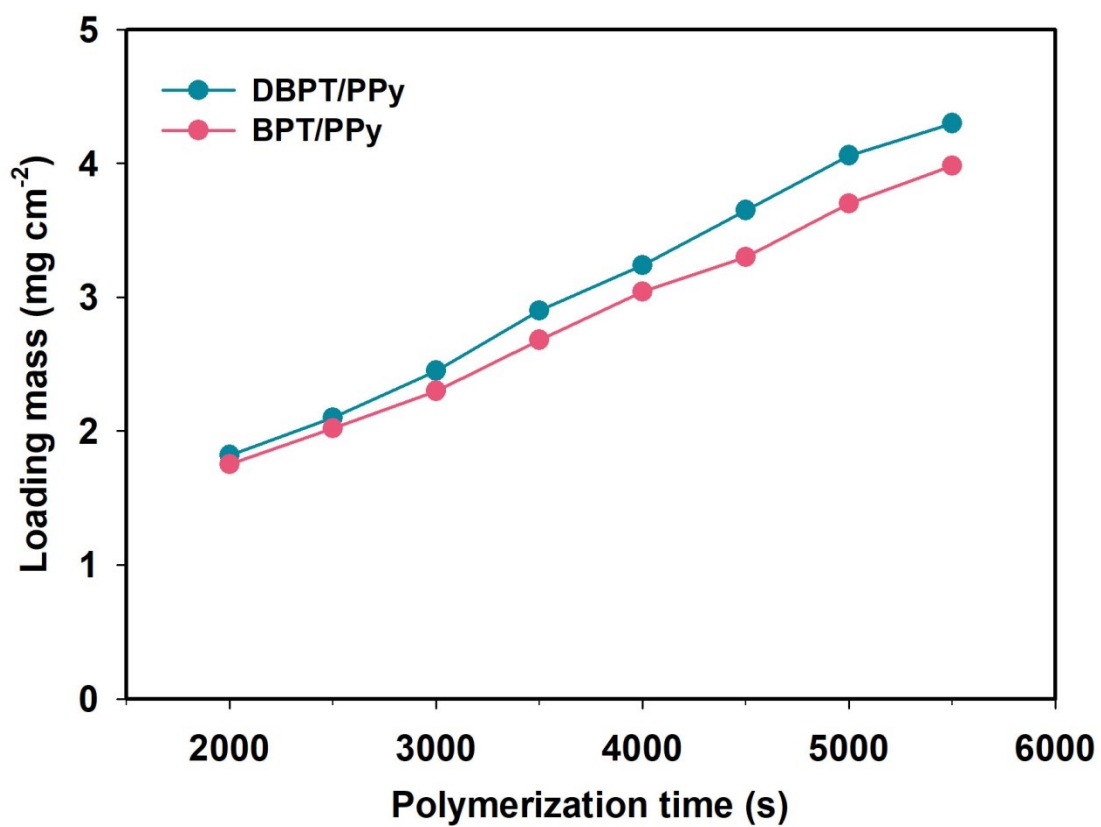**Fig. S7** Schematic of the formed core–shell CNT@PPy composite structure.

Fig. S8 The loading mass of PPy on DBPT/PPy and BPT/PPy electrodes prepared by different electropolymerization time.
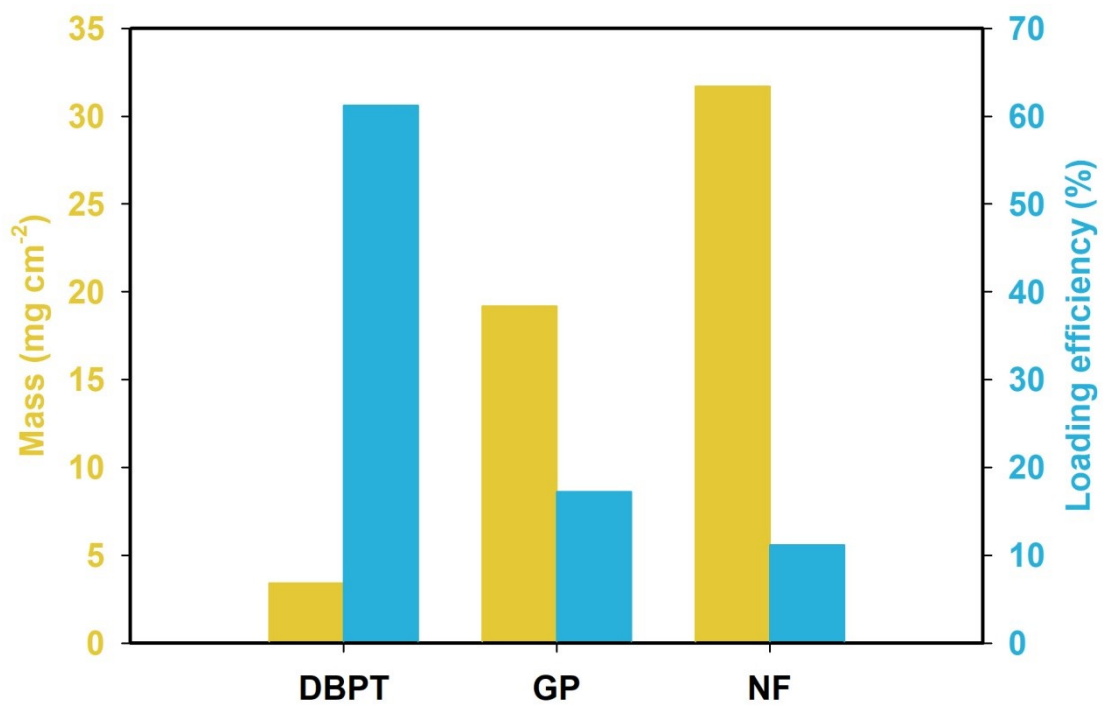
Fig. S9 Mass per unit area and loading efficiency of PPy on the DBPT, GP, and NF electrode substrates.
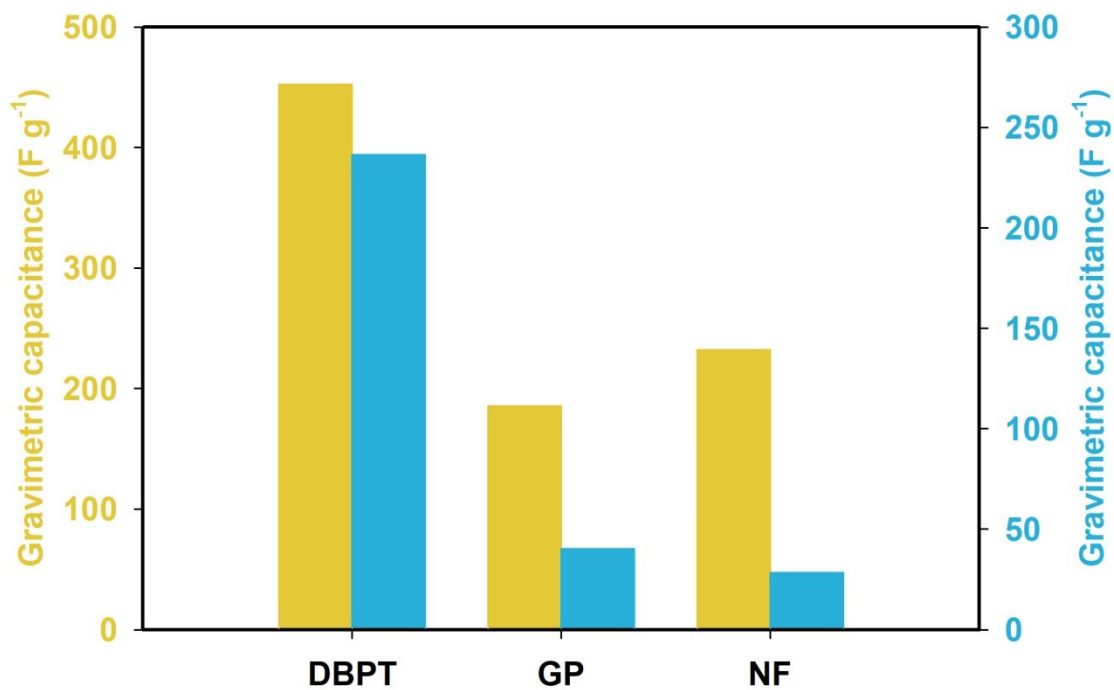
Fig. S10 Gravimetric capacitances calculated with the mass of active materials (left) and entire electrode (right) for the PPy electrodes prepared with DBPT, GP, and NF substrates.
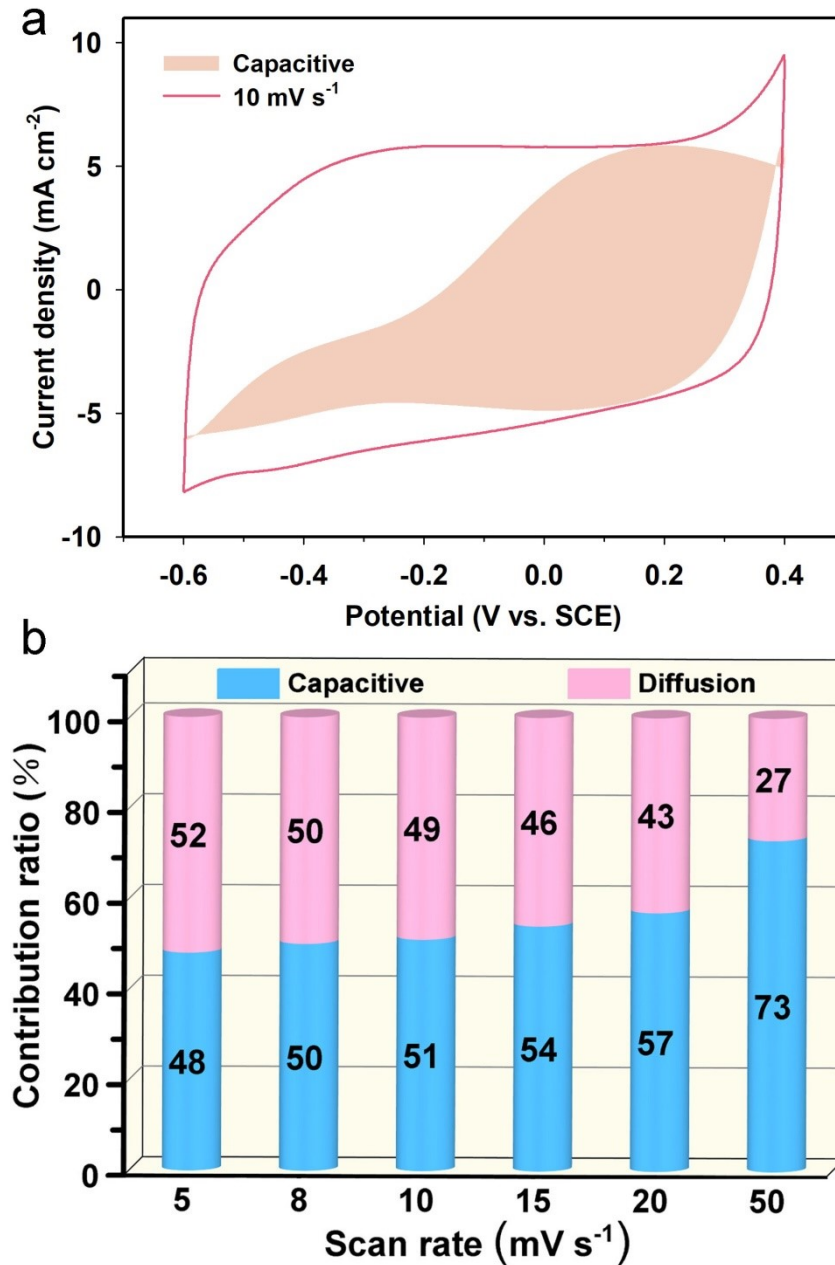
Fig. S11 (a) CV curve with separation between the total current and the capacitive current at 10 mV s^{-1} for BPT/PPy electrode. (b) Separation of capacitive and diffusion-controlled charge-storage contributions at varying CV scan rates.

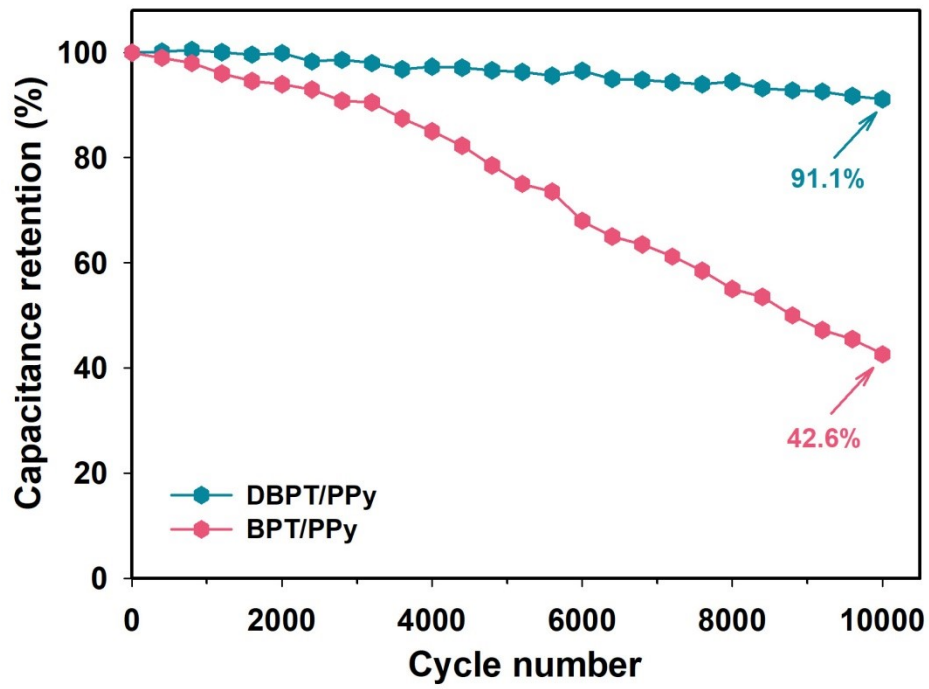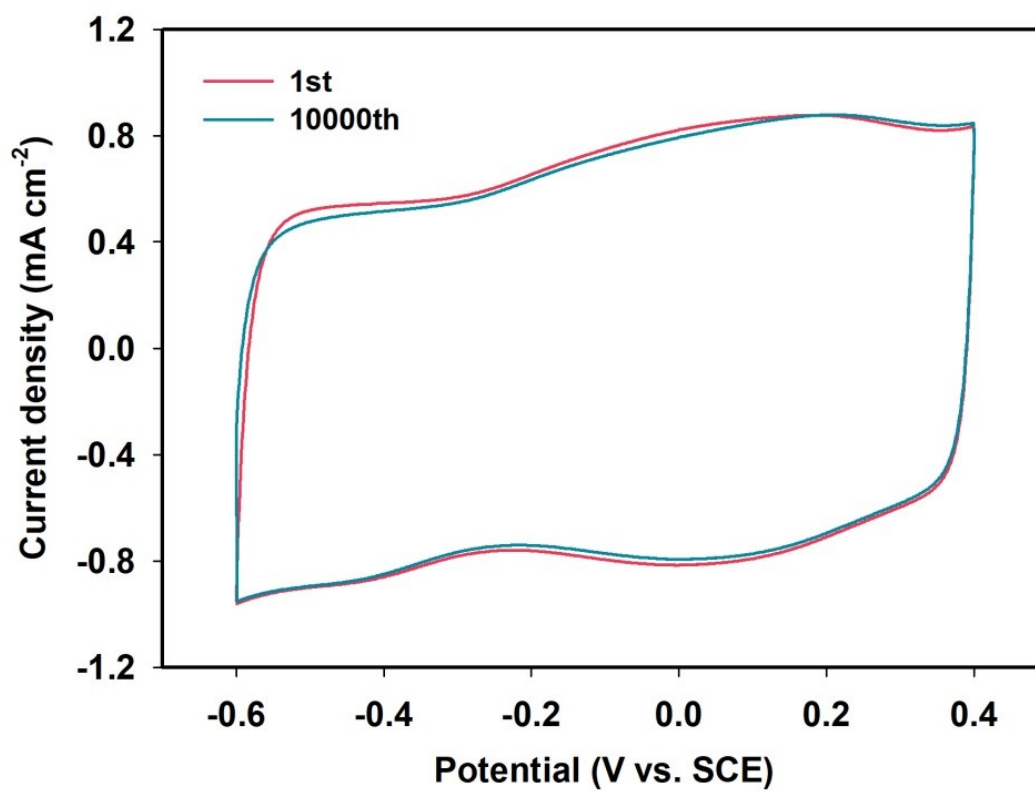**Fig. S12** Comparison of the cycle performance for DBPT/PPy and BPT/PPy electrodes.

Fig. S13 CV curves of DBPT electrode for the 1st and 10000th cycles in 1 M KCl aqueous solution at 80 mV s^{-1}.
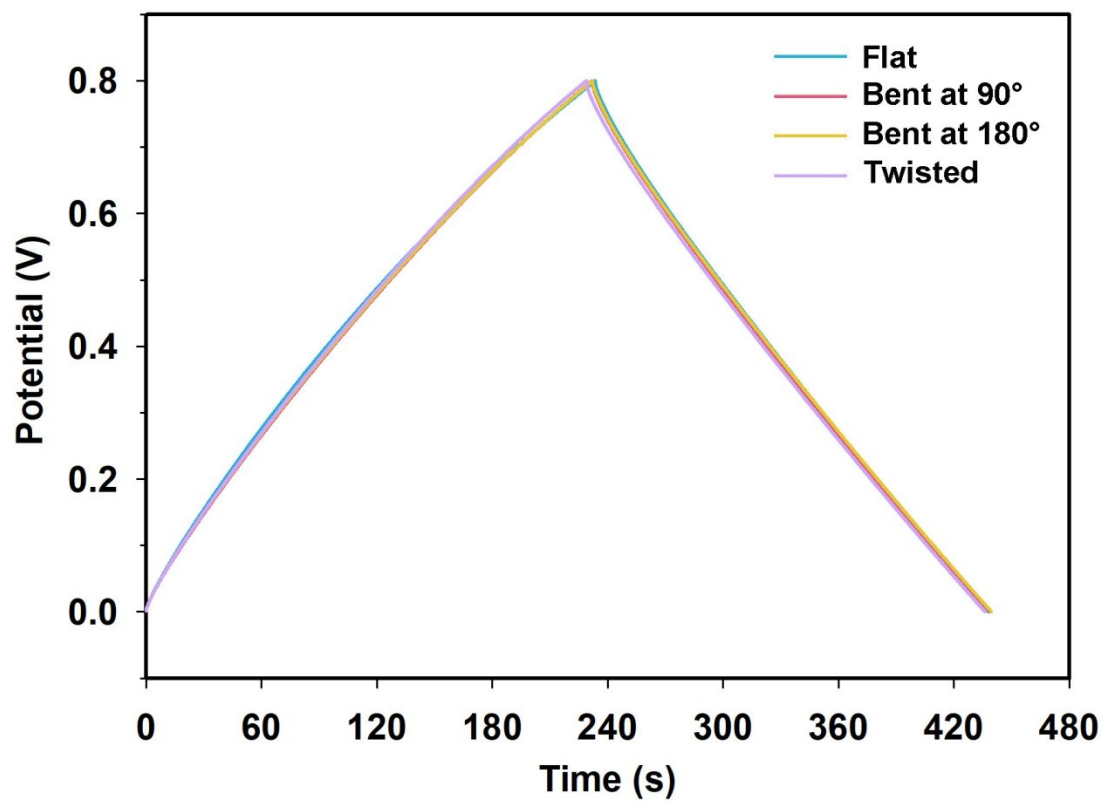
Fig. S14 GCD curves at 2 mA cm^{-2} recorded under varying deformation states for the DBPT/PPy SC.
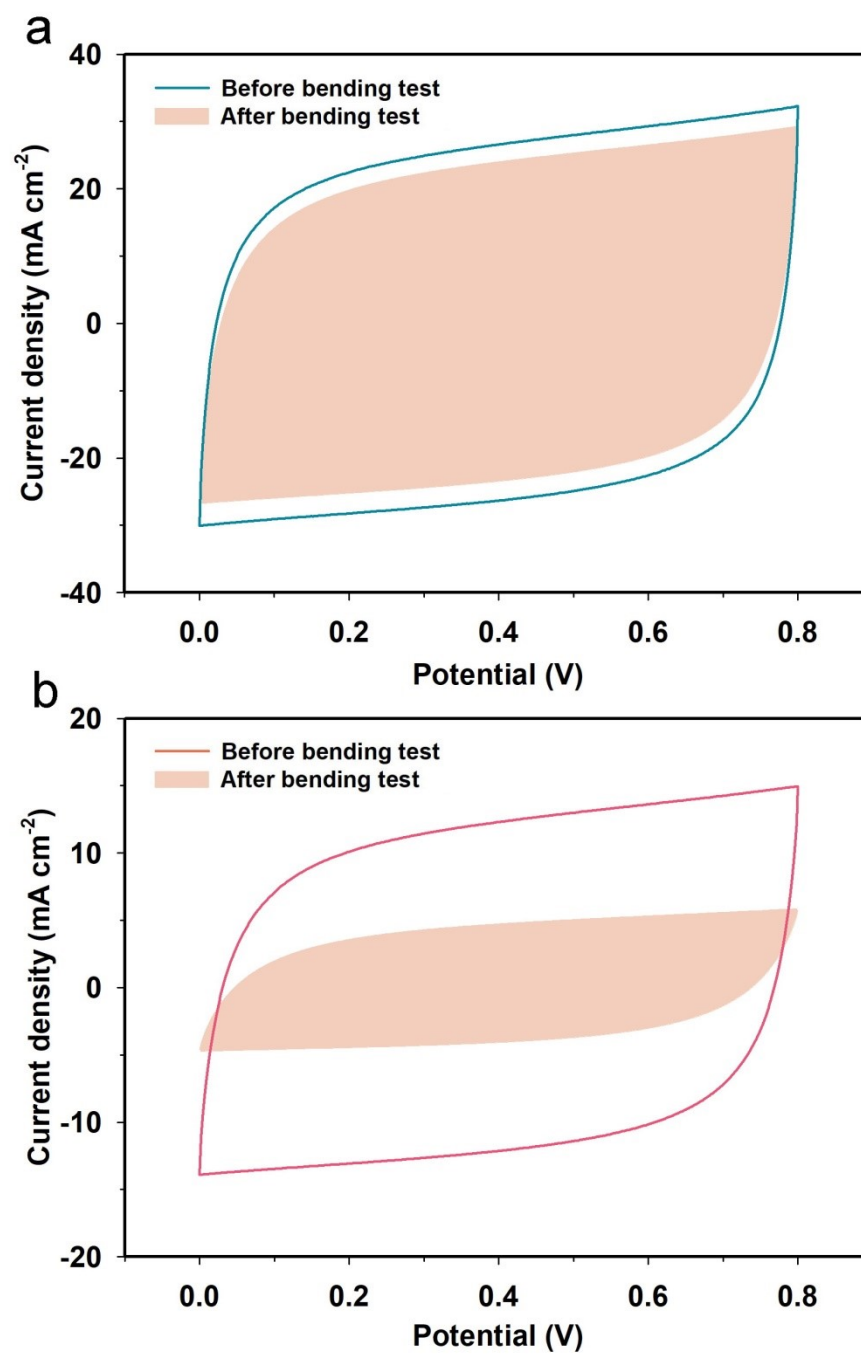
Fig. S15 CV curves at 50 mV s^{-1} of the (a) DBPT/PPy and (b) BPT/PPy SCs before and after bending for 1000 times.

Table S1 Comparison of C_a (mF cm^{-2}) values of the SCs based on CPs reported in the past 3 years.

Electrode material	Test condition	Electrolyte	C_a of SCs	Ref. (year)
PANI:(PA+ARS)/Zr-CFs	1 mA cm^{-2}	1.0 M H$_2$SO$_4$	144.3	S1 (2024)
PANI/S-GO/Cl-GO	10 mV s^{-1}	1.0 M H$_2$SO$_4$	62.45	S2 (2024)
AQS–PEDOT/PAA	1 mA cm^{-2}	H$_2$SO$_4$ - KCl	466.5	S3 (2023)
ACC@MnO$_2$@PEDOT	1 mA cm^{-2}	1.5 M LiCl	334.6	S4 (2023)
V@PANI	5 mV s^{-1}	1.0 M H$_2$SO$_4$	453	S5 (2023)
PEDOT:PSS/RCs	0.2 mA cm^{-2}	PVA-H$_2$SO$_4$	65.55	S6 (2023)
rGO-PANI	0.5 mA cm^{-2}	1.0 M H$_2$SO$_4$	48.83	S7 (2023)
PANI/S-GO/N-GO	10 mV s^{-1}	1.0 M H$_2$SO$_4$	79.7	S8 (2023)
PANI@PPNF	0.05 V s^{-1}	PVA-H$_2$SO$_4$	57	S9 (2022)
PEDOT/MoS$_2$	1 mA cm^{-2}	1.0 M LiClO$_4$	470	S10 (2022)
SiNW/PEDOT@Pt/MnO$_x$	0.5 mA cm^{-2}	PVA-Na$_2$SO$_4$	79.28	S11 (2022)
PANI/PVA/NaCl hydrogel	1 mA cm^{-2}	PVA-H$_2$SO$_4$	247	S12 (2022)
Cu@PPy	5 mV s^{-1}	1.0 M H$_2$SO$_4$	185	S13 (2022)
PANI@Ti$_3$C$_2$T$_x$/PVA	2 A m^{-2}	PVA-H$_2$SO$_4$	103.8	S14 (2022)
SiC@PEDOT	0.05 mA cm^{-2}	2.0 M KCl	6.35	S15 (2021)
MnO$_2$@PEDOT	0.1 mA cm^{-2}	CMC-Na$_2$SO$_4$	33.6	S16 (2021)
AgNFs/MoO$_3$/PEDOT:PSS	0.1 mA cm^{-2}	PVA-LiCl	7	S17(2021)
CC/PPy	0.5 mA cm^{-2}	PVA-H$_3$PO$_4$	75.08	S18 (2021)
PEDOT:PSS	1 mA cm^{-2}	PVA-H$_3$PO$_4$	1.14	S19 (2021)
PEDOT:PSS-LiTFSI-PVA	0.1 mA cm^{-2}	PVA-H$_2$SO$_4$	44.5	S20 (2021)
3D RGO/PANI	5 mV s^{-1}	PVA-H$_2$SO$_4$	31.6	S21 (2021)
C-MWCNT@PANI	1 mA cm^{-2}	PVA-H$_2$SO$_4$	45.4	S22 (2021)
DBPT/PPy	1 mA cm^{-2}	PVA-H$_2$SO$_4$	538.7	This work

References

S1   Z.Y. Chang, D.Q. Liang, S.R. Sun, S. Zheng, K.X. Sun, H.P. Wang, Y.G. Chen, D.L. Guo, H.F. Zhao, L.Z. Sha and W.Y. Jiang, Innovative modification of cellulose fibers for paper-based electrode materials using metal-organic coordination polymers, *Int. J. Biol. Macromol.*, 2024, **264**, 130599.

S2   S. Yasa, O. Kumbasi, M.B. Arvas, M. Gencten, M. Sahin and Y. Sahin, Construction of a ternary composite of S-doped GO, Cl-doped GO, and PANI for coin cell-type asymmetric supercapacitor, *Ionics*, 2024, **30**, 3021-3031.

S3   C. Chen, Y.Q. Li, C.H. Qian, L. Han, Z.C. Lu and L.K. Liu, Boosting PEDOT energy storage with a redox anthraquinone dopant for a flexible hydrogel supercapacitor at sub-zero temperatures, *J. Mater. Chem. C*, 2023, **11**, 7441-7450.

S4   A.R. Akbar, A. Saleem, A. Rauf, R. Iqbal, M. Tahir, G. Peng, A.S. Khan, A. Hussain, M. Ahmad, M. Akhtar, M. Ali, C. Xiong, Q. Yang, G. Ali and F. Liu, Integrated MnO_2/PEDOT composite on carbon cloth for advanced electrochemical energy storage asymmetric supercapacitors, *J. Power Sources*, 2023, **579**, 233181.

S5   B. Ok, M. Gencten, M.B. Arvas and Y. Sahin, One-pot synthesis of vanadium-doped conducting polymers for using as electrode materials of supercapacitors, *J. Mater. Sci-Mater. El.*, 2023, **34**, 1690.

S6   Y. Jeon, Y. Ko, S. Lee, M. Jeong, K. Lee, G. Kwon, J. Kim and J. You, PEDOT:PSS/regenerated cellulose composite microelectrode for high-performance micro-supercapacitor, *Appl. Surf. Sci.*, 2023, **636**, 157806.

S7   W.H. Cho, I.C. Chen and J.Z. Chen, Performance comparison of reduced graphene oxide (rGO)-polyaniline (PANI) supercapacitors with LiCl, Li_2SO_4, and H_2SO_4 electrolytes, *J. Electrochem. Soc.*, 2023, **170**, 010532.

S8   S. Yasa, O. Kumbasi, M.B. Arvas, M. Gencten, M. Sahin and Y. Sahin, S-doped graphene oxide/N-doped graphene oxide/PANI: A triple composite for high-performance supercapacitor applications, *ECS J. Solid State Sci. Technol.*, 2023, **12**, 051002.

S9   H.R. Lai, C.R. Bai, Y.Q. Wang, Z.Y. Fan, Y. Yuan and H. Jiao, Highly crosslinked

conductive polymer nanofibrous films for high-rate solid-state supercapacitors and electromagnetic interference shielding, *Adv. Mater. Interfaces*, 2022, **9**, 2102115.

S10 A.I. Volkov, A.V. Ivanov, A.A. Vereshchagin, J.V. Novoselova, E.G. Tolstopjatova and V.V. Kondratiev, Electrochemical deposition of PEDOT/MoS$_2$ composite films for supercapacitors, *Synth. Met.*, 2022, **285**, 117030.

S11 X.J. Shen, X.Y. Wei, T.F. Wang, S.M. Li and H.T. Li, Solution-processable hierarchical SiNW/PEDOT/MnO$_x$ electrodes for high-performance supercapacitors, *Mater. Chem. Front.*, 2022, **6**, 2894-2904.

S12 S.F. Ye, K.H. Zhu, W.B Ma, L.Y. Dou, P.X. Cui, H. Sha, X.D. Han, X.Y. Wei and X.Y. Tao, Conducting polymer hydrogel driven by sodium chloride as high performance flexible supercapacitor electrode, *J. Electrochem. Soc.*, 2022, **169**, 073501.

S13 B. Ok, M. Gencten, M.B. Arvas and Y. Sahin, Preparation of copper doped conducting polymers and their supercapacitor applications, *ECS J. Solid State Sci. Technol.*, 2022, **11**, 033004.

S14 S.Q. Cao, T.K. Zhao, Y.T. Li, L. Yang, A. Ahmad, T. Jiang, Y. Shu, Z.M. Jing, H.J. Luo, X.F. Lu and H. Zhang, Fabrication of PANI@Ti$_3$C$_2$T$_x$/PVA hydrogel composite as flexible supercapacitor electrode with good electrochemical performance, *Ceram. Int.*, 2022, **48**, 15721-15728.

S15 W.N. Liu, X.X. Li, W.J. Li, Y.M. Ye, H. Wang, P.P. Su, W.Y. Yang and Y. Yang, High-performance supercapacitors based on free-standing SiC@PEDOT nanowires with robust cycling stability, *J. Energy Chem.*, 2022, **66**, 30-37.

S16 Q.C. He, J.J. Ye, Z.Y. Peng, Y.Y. Guo, L.C. Tan and Y.W. Chen, Electrodeposition of poly(3,4-ethylenedioxythiophene) coated manganese dioxide nanospheres for flexible asymmetric planar supercapacitor with superior energy density, *J. Power Sources*, 2021, **506**, 230176.

S17 J. Liang, H.W. Sheng, Q. Wang, J. Yuan, X.T. Zhang, Q. Su, E.Q. Xie, W. Lan and C. Zhang, PEDOT:PSS-glued MoO$_3$ nanowire network for all-solid-state flexible transparent supercapacitors, *Nanoscale Adv.*, 2021, **3**, 3502-3512.

S18 J.H. Liu, X.Y. Xu, C. Liu and D.Z. Chen, Thermal effect on the pseudocapacitive

behavior of high-performance flexible supercapacitors based on polypyrrole-decorated carbon cloth electrodes, *New J. Chem.*, 2021, **45**, 12435-12447.

S19   X. Guan, L.J. Pan and Z. Fan, Flexible, Transparent and highly conductive polymer film electrodes for all-solid-state transparent supercapacitor applications, *Membranes*, 2021, **11**, 788.

S20   J.H. Li, W.R. Yan, G.P. Zhang, R. Sun and D. Ho, Natively stretchable micro-supercapacitors based on a PEDOT:PSS hydrogel, *J. Mater. Chem. C*, 2021, **9**, 1685-1692.

S21   J. Ge, M.S. Zhu, E. Eisner, Y. Yin, H.Y. Dong, D.D. Karnaushenko, D. Karnaushenko, F. Zhu, L.B. Ma and O.G. Schmidt, Imperceptible supercapacitors with high area-specific capacitance, *Small*, 2021, **17**, 2101704.

S22   X. Chu, Z.H. Zhu, H.C. Huang, Y.T. Xie, Z. Xu, Y.H. Wang, C. Yan, L. Jin, Y.C. Wang, H.T. Zhang and W.Q. Yang, Conducting polymer ink for flexible and printable micro-supercapacitors with greatly-enhanced rate capability, *J. Power Sources*, 2021, **513**, 230555.